AIP Journal of Applied Physics

Early time instability in nanofilms exposed to a large transverse thermal gradient: Improved image and thermal analysis

Kevin R. Fiedler and Sandra M. Troian

Citation: Journal of Applied Physics **120**, 205303 (2016); doi: 10.1063/1.4968575
View online: http://dx.doi.org/10.1063/1.4968575
View Table of Contents: http://scitation.aip.org/content/aip/journal/jap/120/20?ver=pdfcov
Published by the AIP Publishing

Early time instability in nanofilms exposed to a large transverse thermal gradient: Improved image and thermal analysis

Kevin R. Fiedler and Sandra M. Troian[a)]
California Institute of Technology, T. J. Watson Sr. Laboratories of Applied Physics, 1200 E. California Blvd., MC 128-95, Pasadena, California 91125, USA

(Received 20 September 2016; accepted 10 November 2016; published online 29 November 2016)

Liquid nanofilms exposed to a large transverse thermal gradient undergo an instability featuring an array of nanopillars whose typical pitch is tens of microns. In earlier works, a comparison of this pitch with the fastest growing wavelength predicted by three different models based on linear instability showed closest agreement with a long wavelength thermocapillary mechanism in which gravity plays no role. Here, we present improved feature extraction techniques, which allow identification of the fastest growing wavelength at much earlier times than previously reported, and more realistic simulations for assessing thermal gradients, which better approximate the actual experimental system. While these improvements lead to better agreement with the thermocapillary mechanism, there persists a quantitative discrepancy with theory which we attribute to a number of experimental challenges. *Published by AIP Publishing.* [http://dx.doi.org/10.1063/1.4968575]

I. BACKGROUND

Liquid films exposed to transverse thermal gradients are known to develop circulatory flow patterns once a critical parameter value is exceeded. For example, a liquid film subject to thermocapillary forces induced by surface thermal gradients will spontaneously transition from a quiescent layer to an organized array of convection cells once the Marangoni number is exceeded. Demonstrations of this phenomenon,[1] known as the Bénard-Marangoni instability,[2,3] have delighted generations for decades. For film thicknesses in the millimeter range or higher, for which hydrostatic forces are important, the convection cells induce slight distortions of the air/liquid interface. These surface deflections are typically observed by seeding the surface with tiny reflecting particles whose motion traces out symmetric surface patterns. Similar surface patterns can arise in even thinner films of the order of 100 μm for which the film thickness is much smaller than the cell separation distance. This limit, described by the long wavelength approximation to the Bénard-Marangoni instability,[4,5] typically still yields small surface deflections since hydrostatic forces remain non-negligible and since in experiment, thermocapillary forces tend to be comparable to capillary forces which repress interfacial curvature.

In the long wavelength limit, the governing dynamics can be reduced to a single fourth order nonlinear partial differential equation describing the spatiotemporal behavior of the air/liquid interface, $h(x, y, t)$, whose behavior can be quantified by examining its modal response to infinitesimal disturbances. Linearization of the interface equation yields a dispersion equation whose positive real part $\beta(|\vec{k}|)$ specifies the rate of growth of linearly independent modes of wave number $|\vec{k}|$. The neutrally stable solution $\beta(|\vec{k}| = 0) = 0$ reflects translational invariance. The solution $\beta(|\vec{k}| = k_c) = 0$ identifies the critical wave number $|\vec{k_c}|$ beyond which surface deflections are damped by capillary and hydrostatic forces. The maximum growth rate $\beta(|\vec{k}| = k_o)$ identifies the fastest growing wavelength, $\lambda_o = 2\pi/k_o$, at early times.

It is often possible to identify the mechanism leading to instability by measuring the characteristic wavelength at early times and comparing the value to λ_o computed from linear stability theory. The length separating adjacent convection cells in macroscopic systems if often measured directly or estimated by Fourier analysis of images obtained by shadowgraphy, particle seeding, or particle image velocimetry. Unfortunately, for the reasons described in this work, such techniques are not feasible in liquid films whose initial thicknesses measure only a few hundred nanometers nor can the temperature drops across such thin films be directly measured either. These challenges have posed difficulties in identifying the competitive forces leading to the spontaneous development of array protrusions in nanofilms, as discussed next.

A. Controversy over the instability mechanism in molten nanofilms

Roughly fifteen years ago, a controversy arose regarding the source of instability in nanoscale liquid films manifest by an array of nanoprotrusions separated by tens of microns. A simplified sketch of the experimental geometry, along with an atomic force microscopy image of the first experiments conducted, is shown in Fig. 1.

It was initially proposed that the periodic nanopillar arrays formed as a result of an induced surface charge (SC) instability.[8,9] Subsequent theoretical and experimental work suggested that the instability might instead be due to an acoustic phonon (AP) mechanism leading to periodic modulation of the acoustic pressure within the film.[10–13] More recent theoretical and experimental work by our group has indicated that the instability represents a new limit of the long wavelength Bénard-Marangoni instability, distinguished by extremely large thermocapillary forces and negligible

[a)]Author to whom correspondence should be addressed. Electronic mail: stroian@caltech.edu. URL: www.troian.caltech.edu

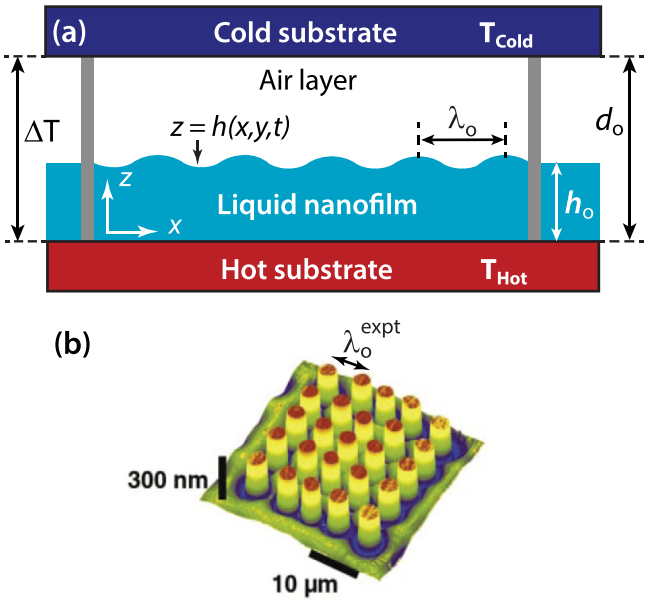

FIG. 1. Simplified geometry of experimental system (not drawn to scale) depicting air/liquid bilayer confined between a hot and cold substrate whose separation distance satisfies the long wavelength condition $d_o \ll \lambda_o$. Typical experimental parameter values[6] are $h_o \approx 50$–400 nm; $d_o \approx 0.1$–$2.5\ \mu$m; $\Delta T = T_{hot} - T_{cold} \approx 10 - 50\,^{\circ}$C; and $\lambda_o^{expt} \approx 10 - 50\ \mu$m. (b) Atomic force microscopy image of *solidified* square array of nanopillars from a 95 nm PMMA film after achieving contact with the cold substrate. Image area approximately $50\ \mu m \times 50\ \mu$m. Height, diameter, and array pitch are 260 nm, $2.7\ \mu$m, and $3.4\ \mu$m, respectively. The actual value of ΔT is unknown. Image reproduced from Deshpande *et al.*, Appl. Phys. Lett. **79**, 1688 (2001). Copyright 2001 AIP Publishing LLC (Fig. 4).[7]

hydrostatic forces, which promotes the growth of 3D protrusions. Numerical studies of the governing equations in this limit[6,14,15] have demonstrated that the thermocapillary stresses rapidly outweigh capillary stresses by several orders of magnitude, allowing film protrusions to grow without bound until contact with the opposing substrate is achieved. Experimental measurements have also confirmed that the characteristic wavelength λ_o varies strongly with the magnitude of the temperature drop across the bilayer film, ΔT, essentially ruling out the surface charge mechanism as the dominant source of instability.[16,17]

In a previous work, we obtained good functional fits between the experiment and the thermocapillary (TC) model prediction for λ_o, but close quantitative agreement seemed to require input values of the liquid thermal conductivity many times larger than reported in the literature. We have since revisited our analysis to ascertain whether this problem can be resolved by making improvements to the image analysis in order to extract λ_o at much earlier times and improvements to the thermal simulations used to assess ΔT. In this current work, we still focus on the dominant Fourier peak from time resolved microscopy images of surface deformations observed in reflection mode to extract the values of λ_o. However, we have implemented more robust image analysis routines to help isolate this main peak at much earlier times during instability. Such early time measurements better conform to the main assumption of linear stability analysis, namely, that interface fluctuations remain very small in comparison to the initial film thickness.

Accurate estimates of ΔT [see Fig. 1(a)] are also required for quantitative comparison to theoretical models. Unfortunately, the bilayer thickness d_o is typically of the order of 1 μm in experiment, a gap too small to allow direct measurement by thermocouple or infrared techniques. Estimates of ΔT are therefore obtained from thermal simulations based on a more complete and more accurate finite element model which more closely mimics the experimental system consisting of thermal conduction through a multilayer structure at steady state conditions. In this current work, we therefore also show how improved simulations result in revised values of ΔT which on average are half as large than previously reported.[16]

In what follows, we describe the improved image analysis for isolating the fastest growing mode and a more accurate thermal model for assessing the temperature drop across the confined air/nanofilm bilayer. Feature extraction at much earlier times, coupled with more realistic thermal simulations, leads to a better overall functional and quantitative agreement with the thermocapillary model. Despite these improvements, there persists a quantitative discrepancy with theory which we attribute to a number of experimental challenges.

II. LINEAR STABILITY PREDICTIONS FOR THE WAVELENGTH OF THE FASTEST GROWING MODE

We first briefly review the predictions for λ_o arising from three different physical models, namely, the induced surface charge (SC), acoustic phonon (AP), and thermocapillary (TC) models. These predictions derive from a modal linear stability analysis of the governing interface equation for $h(x, y, t)$ in the long-wavelength limit $d_o \ll \lambda_o$ where hydrostatic forces play no role and the liquid viscosity is assumed constant since the amplitude of surface deflections at early times is very small. Listed in Tables I–III are the analytic expressions for λ_o normalized by the initial film thickness h_o, along with key system dimensions and material constants from experiments reported in the literature. The complete derivations and additional experimental information can be found in the references cited. A review of the original experiments conducted by various groups, along with a discussion of the challenges and deficiencies of each, can be found in Ref. 6. As evident, the SC instability is independent of the temperature drop ΔT, which disagrees

TABLE I. Normalized wavelength for the fastest growing mode in the induced surface charge (SC) model.[8,9] Listed are the relevant system dimensions and material constants for low molecular weight poly(methylmethacrylate) (PMMA 2 kg/mol) films heated to 130 °C used in experiment.

$$\frac{\lambda_o^{SC}}{2\pi h_o} = \sqrt{\frac{2\varepsilon_o \varepsilon_p^2 \gamma h_o}{\sigma^2 d_o^2}}\left(\frac{d_o}{h_o} + \frac{1}{\varepsilon_p} - 1\right)^{3/2}$$

h_o	Initial film thickness	50–103 nm
d_o	Substrate separation distance	180–640 nm
λ_o	Fastest growing wavelength	2–8 μm
ε_o	Vacuum permittivity	8.85×10^{-12} F/m
ε_p	PMMA permittivity	3.5
γ	PMMA surface tension	30 mN/m
σ	Interfacial charge density	10^{-3} mC/m^2

TABLE II. Normalized wavelength for the fastest growing mode in the acoustic phonon (AP) model. Listed are the relevant system dimensions and material constants for high molecular weight polystyrene (PS 108 kg/mol) films used in experiment.[10–13]

$$\frac{\lambda_o^{AP}}{2\pi h_o} = \sqrt{\frac{\gamma u_p}{\bar{Q}(1-\kappa)k_a \Delta T}}\left(\frac{d_o}{h_o} + \kappa - 1\right)$$

h_o	Initial film thickness	80–130 nm
d_o	Substrate separation distance	100–600 nm
λ_o	Fastest growing wavelength	1–10 μm
ΔT	Temperature differential	10–55 °C
γ	PS surface tension	30 mN/m
u_p	Speed of sound in PS	1850 m/s (Ref. 18)
$\bar{Q}$	Acoustic phonon coefficient	6
k_a	Air thermal conductivity	34 mW/m °C (Ref. 18)
k_p	PS thermal conductivity	160 mW/m °C
κ	Thermal conductivity ratio k_a/k_p	0.213

with experimental measurements.[11,16] In what follows, we therefore exclude this model from consideration and only explore differences between the AP and TC models.

Experiments to date have used either polystyrene (PS) or poly(methylmethacrylate) (PMMA) films spun coat onto a silicon wafer to produce a flat and uniform film then melted *in situ*. The main advantage to using polymer films is that their low glass transition temperatures[21] facilitate rapid melting and solidification. Estimates of the shear rates incurred in experiment yield very small Deborah numbers, indicating that non-Newtonian effects play no role at early times and that the liquid film can be modeled as a simple Newtonian fluid. All three models therefore assume that the film viscosity is independent of the shear rate. However, the viscosity of polymers depends strongly on temperature. While this dependence ultimately slows the late time growth of protrusions as they approach the opposing cold substrate, it is not expected to affect early time growth when surface deformations are of the order of tens of nanometers or less. All three models therefore assume that the relevant film viscosity for the linear stability analysis is constant and equal to the temperature of the supporting substrate.

The expression for λ_o in the acoustic phonon model (AP) in Table II relies on the constant $\bar{Q}$, the so-called acoustic quality factor, which arises from phonon transmission and reflection from the three interfaces comprising the bilayer system, namely, the silicon/polymer, the air/polymer, and air/silicon surfaces. Positive values of $\bar{Q}$ lead to film destabilization and protrusion growth. In all experiments conducted so far, the value of $\bar{Q}$ has been treated as a fitting parameter. The remaining material constants, namely, the liquid film surface tension, γ, and thermal conductivity of the air and liquid film, have been obtained from literature values. In the AP model then, the normalized wavelength of the fastest growing mode increases linearly with the normalized substrate separation distance $D \equiv d_o/h_o$.

TABLE III. Normalized wavelength for the fastest growing mode in the thermocapillary model.[6,14–16] Listed are the relevant system dimensions and material constants for low molecular weight polystyrene (PS 1.3 kg/mol) films used in experiment.

$$\frac{\lambda_o^{TC}}{2\pi h_o} = \sqrt{\frac{4\gamma}{3\kappa|\partial\gamma/\partial T|\Delta T}}\left(\sqrt{\frac{d_o}{h_o}} + (\kappa - 1)\sqrt{\frac{h_o}{d_o}}\right)$$

h_o	Initial film thickness	95–390 nm
d_o	Substrate separation distance	605–2360 nm
λ_o	Fastest growing wavelength	27–68 μm
ΔT	Temperature difference	16–44 °C
γ	Surface tension (100 °C)	33 mN/m (Ref. 19)
k_a	Air thermal conductivity (80 °C)	30 mW/m °C (Ref. 20)
k_p	PS thermal conductivity (100 °C)	128 mW/m °C (Ref. 19)
κ	Thermal conductivity ratio k_a/k_p	0.234
$\lvert\partial\gamma/\partial T\rvert$	Surface tension coefficient	78 μN/m °C (Ref. 19)

The expression for λ_o in the thermocapillary (TC) model in Table III also relies on the liquid film surface tension, γ, the magnitude of the surface tension coefficient, $|\partial\gamma/\partial T|$, and the air and liquid thermal conductivity, all values also obtained from the literature. In contrast to the AP model, however, the normalized wavelength of the fastest growing mode increases with the normalized substrate separation distance D according to $\sqrt{D} + (\kappa - 1)/\sqrt{D}$. While the original experiments[10–13] were designed to probe values of $D \lesssim 5$, the experiments reported in Ref. 16 and reanalyzed in this work allowed access to a larger range $D \lesssim 25$. This feature, coupled with the ability to view the film instability *in-situ*, has allowed more accurate measurements of λ_o for several reasons, including rejection of runs suffering from non-parallel substrates or defective films containing pinholes, embedded or surface contaminant particles.

Prior work[6] outlined the challenges inherent in making direct comparison between theory and experiment. The biggest problem of all is that the majority of experiments prior to 2011 reporting measurements of λ_o had little to do with the actual instability in that the formations were allowed to grow, make contact with the opposing substrate, and solidify in place before the cold substrate was removed and measurements of λ_o taken. Measurements obtained in this way not only violate the assumptions of linear stability theory but also include influences and effects not incorporated into the theoretical analysis. For example, contact of a warm protrusion with the opposing cold substrate tends to induce coalescence of adjacent protrusions followed by flow migration along the underside of the cold substrate, both of which strongly affect the final measured values of λ_o. Film shrinkage during solidification can also play a role. For accurate comparison to model predictions for λ_o, the amplitude of features which emerge from an initial flat air/liquid interface must be infinitesimally small. In this work, we focus exclusively on estimates of the instability wavelength measured at the earliest possible time, given the experimental setup and other limitations described.

The remainder of this work is divided as follows. In Sec. III, we briefly review some details of the experimental apparatus used in Ref. 16, from which the raw images analyzed in this current work were obtained. In Sec. IV, we outline significant improvements to the image analysis and processing routines which lead to more accurate measurements of λ_o at much earlier times than those reported in Ref. 16. In Sec. V, we detail a new finite element model used to extract more accurate estimates of ΔT which better mimics the experimental system. These two improvements lead to better overall agreement with the thermocapillary model.

We conclude by examining some persistent deficiencies, however, which are traceable to uncertainties in measurement of key parameters needed to make contact with theory.

III. BRIEF DESCRIPTION OF EXPERIMENTAL SETUP

We review some key aspects of the experimental setup shown in Fig. 2. More extensive discussion, including sample preparation procedures, can be found in Ref. 16. The resistive heating element used to enforce the temperature differential ΔT across the bilayer film consisted of an indium tin oxide (ITO) coated glass slide. The current passed through the ITO layer for increasing the overall thermal flux was regulated via a proportional integral derivative (PID) feedback control. Heat loss beneath the glass slide was minimized by a thin layer of fiberglass insulation. The thermal sink used to draw heat vertically and away from the air/liquid bilayer consisted of a thin copper sheet (Cu) in contact with a chiller loop perforated with a small cylindrical viewing port. Strong suction was applied to the region beneath the glass coverslip (i.e., vacuum region) to enforce good contact between the sapphire disk and cold Cu sheet. The heat sink enforced through the chiller loop and the thinness of the interstitial material layers guaranteed that the dominant heat flux traversing the layered stack was due to conduction and not convection or radiation. (In Sec. V, we provide estimates of the thermal flux due to thermal conduction, convection, and radiation and conclude that conduction is dominant.)

In most of the experimental runs listed in Table VII, the underside of the sapphire window was patterned with a transparent cylindrical disk of SU-8. This cooled disk helped trigger and localize the instability to the region directly below the disk where the nominal temperature gradient, $\Delta T/d_o$, was largest. The thickness of the air layer above the nanofilm was enforced by four SU-8 spacers patterned onto the sapphire disk. In each run, two thermocouples were used to measure T_+ (beneath the exterior edge of the silicon wafer) and T_- (top surface of the Cu layer just beyond the glass coverslip). Time stamped color images of reflections from the liquid surface were captured by a CCD camera at 10× magnification. Tables VI and VII list all relevant dimensions, operating conditions, material constants, and numerical estimates of ΔT for all runs analyzed.

In the experiments which provided the raw images reanalyzed in this work,[16] a polymer coated silicon wafer was inserted into the assembly prior to a run and the opposing hot and cold substrates leveled and made parallel by adjusting external screws until interference fringes observed were all but eliminated. Data collection began once power was delivered to the indium tin oxide (ITO) slide, which set the origin of time for each run. Thereafter, images were captured at regular intervals, typically between 20 s and 2 min, depending on the flow speed generated and the rapidity with which protrusions grew. To ensure that the temperature drop ΔT had reached steady state conditions before any measurements of λ_o were initiated, the rise time to reach T_+ was monitored. Depending on the power applied, the rise time ranged from 1.5 to 5 min, only after which were measurements of λ_o recorded.

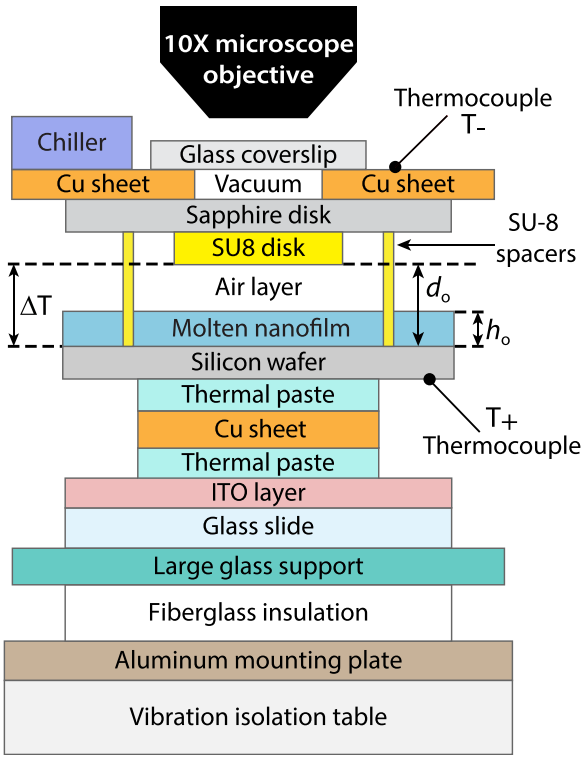

FIG. 2. Diagram of the experimental setup[16] illustrating the many layers affecting heat transfer throughout the system (not drawn to scale). Dimensions and thermal conductivities of each layer are listed in Table VI. Designated temperature readings, T_+ and T_-, were registered using small thermocouples and used to calibrate boundary temperatures in the finite element simulations described in Sec. V.

IV. ESTIMATES OF THE FASTEST GROWING WAVELENGTH FROM IMPROVED IMAGE ANALYSIS

Accurate measurement of the instability wavelength at early times requires feature extraction from rather noisy images which appear featureless to the naked eye. Here, we describe the various steps used to facilitate identification of emergent structure formation.

A. Image analysis protocol

The color image sequences for each experimental run were first separated into three color channels (RGB)—the channel exhibiting the highest contrast was selected for analysis. Typically, the blue channel offered highest contrast—see Table VII. Image subtraction was then carried out to reduce image noise, especially problematic at early times, or to eliminate obvious artifacts such as stationary dust particles on any of the optical components. For each image sequence, a reference image captured at time t_{ref} was selected and subtracted from all subsequent images. This reference image was always obtained after the thermocouple registering the value T_+ had reached the desired set point and the color of the nanofilm had stabilized. (The ITO coated slide typically required several minutes to achieve steady state after the power was applied.) The mean intensity of each image was then computed and that value subtracted from each image to yield a mean intensity of zero. This step eliminated the zero wave number Fourier component which sometimes occluded the peak of interest associated with the instability.

B. Extraction of λ_o from power spectra

The 2D discrete Fourier transform for each image in a run sequence was then computed using a 2D fast Fourier transform routine.[22] The data were radially averaged by first segmenting the image into concentric rings of width $\Delta k = 2\pi/L_i$, where L_i denotes the smaller of the raw image dimensions given in Table VII, and then averaging the Fourier components within each ring. The corresponding power spectrum, i.e., modulus squared of the Fourier coefficients, was then re-scaled in amplitude so that the maximum peak value of the final image in chronological order was equal to one. This step ensured that the Jacobian values generated during the nonlinear regression were well-conditioned—otherwise, large Fourier amplitude coefficients tended to overwhelm and distort the peak fitting parameters. The resulting scaled data were then fit to the curve $G[k(t)]$ given by Eq. (1), which represents the sum of a Lorentzian peak with an exponentially decaying background, according to which

$$G[(k(t)] = f_o(t)\,\frac{a^2(t)}{a^2(t)+[k(t)-k_o(t)]^2} + f_1(t)\,e^{-b(t)k(t)} + f_2(t), \tag{1}$$

where $k(t) = |\vec{k}(t)|$ and t denotes time. The fitting parameters describe a Lorentzian peak amplitude $f_o(t)$ with half-width at half-maximum $a(t)$ centered about the wave number $k_o(t) = |\vec{k_o}(t)|$ summed with an exponential curve of amplitude $f_1(t)$ and decay constant $b(t)$ (associated with the background intensity). The value $f_2(t)$ was used to set the vertical offset. The contribution from the decaying exponential is typical of spectral leakage which occurs when periodic extension of the observation window imposed on the fundamental image does not match the periodicity (or lack thereof) of the structure in the fundamental image.[23] Good fits were obtained by analyzing images in reverse chronological order since the peak value $k_o(t)$, the most sensitive parameter in the nonlinear fitting process, was usually easily identifiable. Additionally, iteration on the fitting parameters proceeded more quickly by using the spectral curve fitting parameters at time t_{n+1} as initial estimates for the fitting parameters at the earlier time t_n.

The initial parameter values for the fitting routine generally fell into two categories—either the Lorentzian peak dominated the exponentially decaying background or else the exponential background was comparable or even larger than the Lorentzian peak amplitude. Correspondingly, the initial seed for the amplitude of the Lorentzian, f_o, was set to be much larger than f_1, i.e., 1.0 versus 0.1. Else, the initial seed values were reversed, i.e., $f_o = 0.2$ and $f_1 = 5.0$. The initial guesses for the peak half-width at half-maximum, $a(t)$ and decay value $b(t)$, were usually chosen to be 0.03 and 10, respectively—these values showed only weak dependence on the initial choices for f_o and f_1. The final parameter values for the nonlinear fitting routine for the image sequences shown in Figs. 3(d) and 4(d) can be found in Tables IV and V.

On occasion, the automated fitting routine ran into problems of numerical overflow or division by zero, mostly for

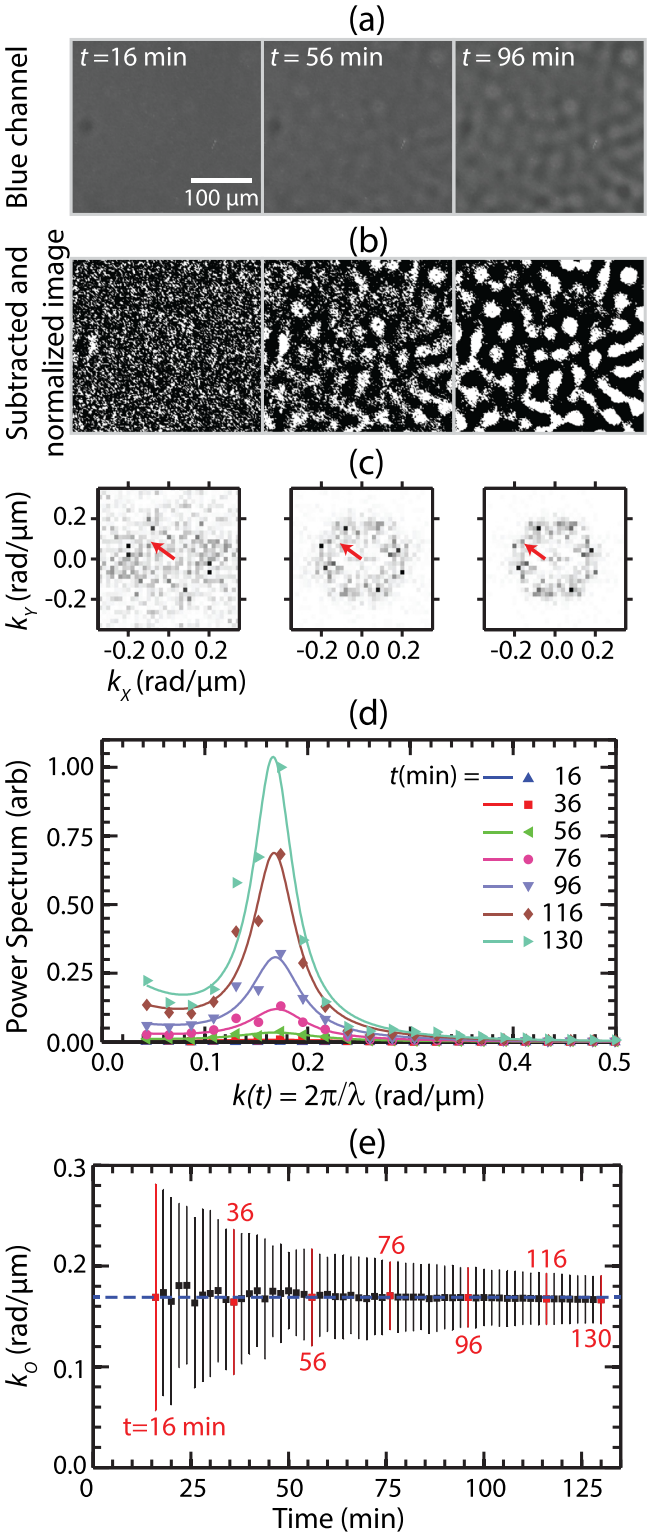

FIG. 3. Representative images of structure formation in an initially flat and uniform PS nanofilm for experiment #56 in Table VII. (a) Grey scale images from the blue channel for times $t = 16$ min, 56 min, and 96 min. (b) Corresponding gray scale images after subtraction of reference image $t_{ref} = 4$ min and zeroing of mean intensity value. (c) Corresponding normalized power spectra. Red arrow denotes the wave number $\vec{k_o}(t)$. (d) Data and fit curves for the radially averaged power spectra during instability and growth. (e) Peak wave number $k_o(t)$—dashed line represents initial value. Vertical bars represent the peak full width at half maximum, namely, $2\,a(t)$. The wave number at $t = 16$ min equals $k_o = 0.169\ \mu m^{-1}$, corresponding to a fastest growing wavelength $\lambda_o = 37.2\ \mu m$.

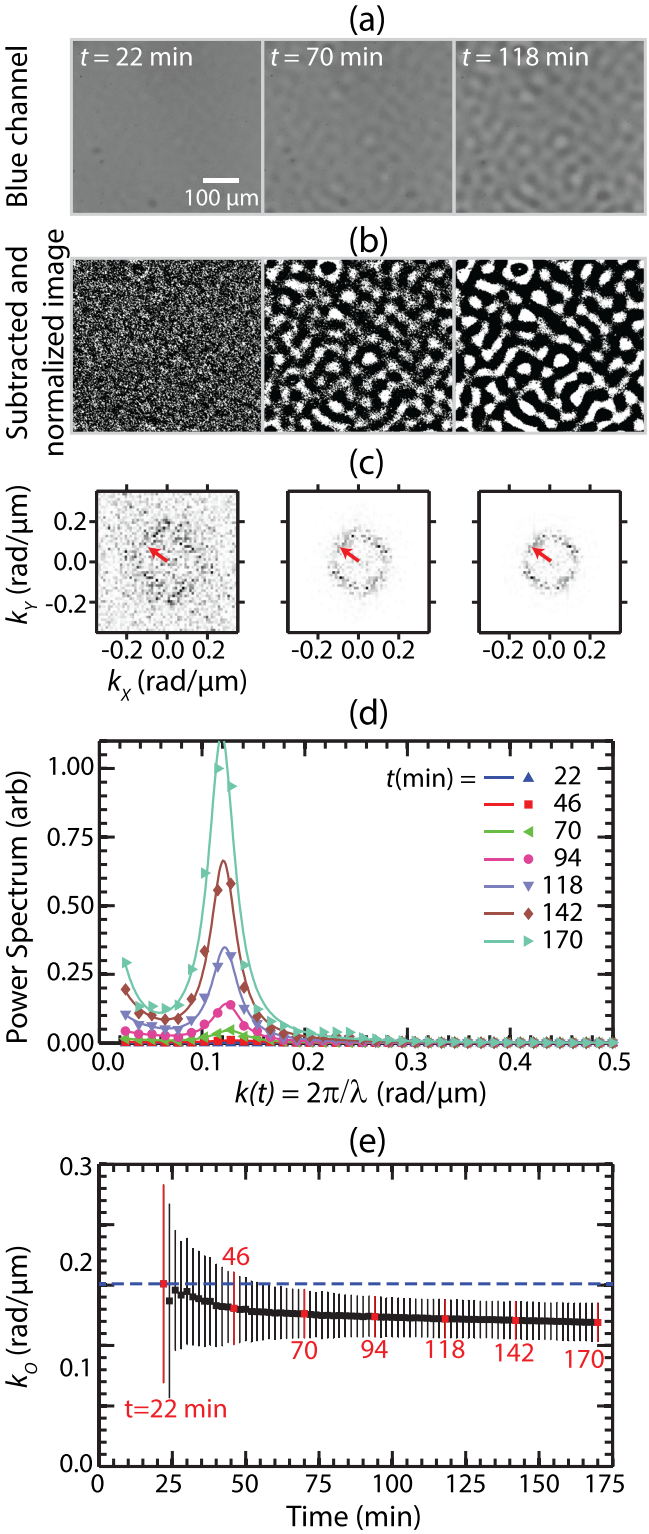

FIG. 4. Representative images of structure formation in an initially flat and uniform PS nanofilm for experiment #69 in Table VII. (a) Grey scale images from the blue channel for times $t = 22$ min, 70 min, and 118 min. (b) Corresponding gray scale images after subtraction of reference image $t_{ref} = 14$ min and zeroing of mean intensity value. (c) Corresponding normalized power spectra. Red arrow denotes the wave number $\vec{k}_o(t)$. (d) Data and fit curves for the radially averaged power spectra during instability and growth. (e) Peak wave number $k_o(t)$—dashed line represents initial value. Vertical bars represent the peak full width at half maximum, namely, $2a(t)$. The wave number at $t = 22$ min equals $k_o = 0.151\ \mu m^{-1}$, corresponding to a fastest growing wavelength $\lambda_o = 41.6\ \mu m$.

TABLE IV. Fit parameters according to Eq. (1) for the curves shown in Fig. 3(d).

Time (min)	$f_o \times 10^2$	$a \times 10^2$ (1/μm)	k_o (1/μm)	$f_1 \times 10^2$	b (μm)	$f_2 \times 10^4$
16	0.121	11.2	0.169	0.115	47.8	3.08
36	0.767	7.21	0.164	2.78	40.7	4.12
56	3.26	4.80	0.169	1.24	13.2	3.69
76	11.3	3.34	0.171	3.51	9.27	0.235
96	29.5	2.93	0.169	8.13	10.4	−7.08
116	66.4	2.55	0.168	18.5	12.0	−14.7
130	101	2.37	0.167	31.2	13.9	−12.2

images obtained at very early times, well before any features were discernible by the naked eye. In such cases, the routine was re-initiated using a new set of parameter values for which the amplitude of the Lorentzian peak and the exponential background were set equal to the maximum of the spectral curve. The nonlinear fitting routine then converged on a successful fit even in the absence of a Lorentzian-like peak. Consequently, a set of selection criteria were established to define a valid peak fit. If a peak could not be reliably extracted no matter the initial parameter values, then that data point was discarded and the next image analyzed. Finally, the values of $k_o(t) = 2\pi/\lambda(t)$ were plotted in time and the earliest valid fit identified as λ_o. These improvements over the original analysis[16] led to more accurate and reproducible fits. More significantly, these enhancements produced measurement of the fastest growing wavelength at much earlier times than previously reported—see Fig. 6(b) for a direct comparison. In the absence of any defects or other spurious features, only a single peak appeared in the power spectra at early times, which greatly simplified the analysis. For most but not all runs, the location of that peak remained relatively fixed in time, yielding a fairly constant value of k_o. In some cases, we did observe a slight decrease in k_o in time, as discussed next. In other cases, late time analysis was complicated by the appearance of interference fringes arising from taller protrusions, either from instability growth or coalescence of neighboring fluid mounds. These images were discarded since they could not be analyzed by the procedure described.

C. Application of image processing routines to sample runs

Shown in Fig. 3 for experiment #56 are the results of the image processing routine used to extract the value of λ_o.

TABLE V. Fit parameters according to Eq. (1) for the curves shown in Fig. 4(d).

Time (min)	$f_o \times 10^2$	$a \times 10^2$ (1/μm)	k_o (1/μm)	$f_1 \times 10^2$	B (μm)	$f_2 \times 10^4$
22	0.0386	8.21	0.151	…	…	12.2
46	0.949	3.01	0.131	0.939	36.0	1.90
70	4.45	1.99	0.126	2.70	25.3	2.47
94	13.8	1.67	0.124	6.85	21.6	2.42
118	34.3	1.57	0.122	19.8	29.6	0.784
142	65.9	1.55	0.121	44.7	37.6	−3.26
170	112	1.59	0.119	108	56.4	−10.4

Experimental information relevant to that particular run can be found in Table VII. Fig. 3(a) depicts three grey scale images from the blue channel for times $t = 16$ min, 56 min, and 96 min which illustrate structure formation at early, intermediate, and late times. Fig. 3(b) shows these images after subtraction and zeroing of the mean intensity value. (The images shown in Fig. 3(b) have been rescaled in amplitude with MATLAB routine Imadjust[22] to maximize contrast for visualization purposes only.) These first two steps helped maximize contrast of embedded structure formation, none evident to the naked eye. Fig. 3(c) shows the corresponding 2D Fourier transforms. Plotted in Fig. 3(d) are the radially averaged power spectral curves—the fit parameters can be found Table IV. The two earliest curves exhibit a very broad peak indicative of film isotropy as evident in the left panel of Fig. 3(b). From $t = 56$ min onwards, a sharp peak begins to develop. Inspection of images at $t = 56$ min and 96 min indicates emergent hexagonal order which produced six darker spots decorating the main ring in the middle and right panels of Figs. 3(b). Numerical simulations for the late time behavior of the thermocapillary model[6] have shown that the onset of the *nonlinear regime* is characterized by such hexagonal order. Plotted in Fig. 3(e) are the extracted values for $k_o(t)$ spanning the linear to nonlinear regime. The earliest value extracted, here $t = 16$ min, was identified with the instability wavelength, $\lambda_o = 2\pi/k_o$. The majority of experiments tended to generate fairly constant values of $\lambda_o(t)$ even beyond the linear regime, as illustrated by the curve in Fig. 3(e).

Occasionally, the initial value $k_o(t)$ was observed to decrease in time before leveling off to a constant value. Shown in Fig. 4 is a representative example from experiment #69. Inspection of the 2D Fourier transform in Fig. 4(c) reveals late time structure formation more closely resembling square and not hexagonal ordering. Numerical simulations for the late time behavior of the thermocapillary model[6] have shown that non-parallel substrates, which introduce an additional unintended lateral thermal gradient, can generate nanopillar arrays exhibiting fourfold and not sixfold symmetry. This effect might help explain the observed decrease in $k_o(t)$ in Fig. 4(e). Nonetheless, the value used to compare with theoretical models was chosen to be the wavenumber at earliest time for which a Lorentzian peak could be identified, in this case the value of $k_o(t = 22\,\text{min})$.

D. Complications incurred by film defects

Embedded or exposed defects in liquid nanofilms compromise film uniformity by causing local film thickening. While such defects are always a nuisance, they cause special problems in experiments with nanofilms due to the more rapid growth of thicker regions exposed to a large thermal gradient. Such growth, however, arises from a nucleation and growth process and not linear instability. While contaminant particles that appear on the surface of optical components or the sapphire window could be easily removed from view by image subtraction, defects integral to the thin liquid film could not so easily be removed since their presence tended to induce periodic film undulations nearby. In general, such defective films were either excluded from analysis or else the analysis was restricted to smaller defect-free regions far from the offending site. The latter, of course, tended to increase noise since the sample image size for analysis was smaller still.

The two most common defects observed in spun coat PS films are illustrated in Fig. 5(a). Embedded defects tended to produce isolated thickened regions encapsulating contaminants. Exposed defects produced ring-like elevations. Both caused film undulations in regions adjacent to the defect especially once the liquid got drawn toward the cold substrate. Shown in Fig. 5(b) are two gray scale images extracted from the green color channel for experiment #62 at time $t = 10$ min. Fig. 5(c) shows the corresponding images after subtraction by the reference image at $t_{\text{ref}} = 3$ min and zeroing of the mean intensity value. The image on the left shows structure formation as a result of the instability while the image on the right shows the evolution of the instability modified by the presence of a large dewetted hole caused by an exposed particulate. A comparison of the two radially averaged and normalized Fourier transforms are shown in Fig. 5(d). Since the areas analyzed were small (see Table VII), defects had a pronounced effect on the characteristic wavelength λ_o extracted from the Lorentzian peak. The background intensity amplitude due that defect was large, which therefore led to much larger Fourier components and therefore more background noise. This effect remained a problem even when the image size was larger.

In this particular run shown, the wave number for the defect free region at $t = 10$ min was measured to be $k_o = 0.164\,(\mu\text{m})^{-1}$ for a value $\lambda_o = 38.4\,\mu$m, while that for the exposed defect region was measured to be $k_o = 0.216\,(\mu\text{m})^{-1}$ for a value $\lambda_o = 29.1\,\mu$m. Closer inspection revealed that exposed and embedded defects induced local ordering and growth in adjacent regions of the film, both of which interfered with measurement of the native instability wavelength. As a result, sequences or portion of sequences containing defects were eliminated from analysis.

E. Results of λ_o from enhanced image analysis

Shown in Fig. 6(a) is a direct comparison of λ_o values obtained from the current and original study.[16] Fig. 6(b) shows a direct comparison of the times at which those values were extracted. The analysis procedure enhanced feature extraction, which in turn allowed identification λ_o at earlier times. Shown in Fig. 6(c) is a comparison of the original and current data sets for the normalized quantity $\lambda_o(\Delta T)^{1/2}/h_o$ versus the normalized separation distance $D = d_o/h_o$ against the predictions of the AP (dashed line) and TC (solid curve) models, whose expressions are given in Tables II and III and Eqs. (2) and (3). Here, the coefficients C_{AP} and C_{TC} were treated as fit parameters. In that figure, the input values for ΔT are those estimates computed from the *original* thermal simulations,[16] which are labeled ΔT^{orig} in Table VII. (In Sec. V, we describe improvements to the thermal simulations leading to revised current values ΔT^{curr}.)

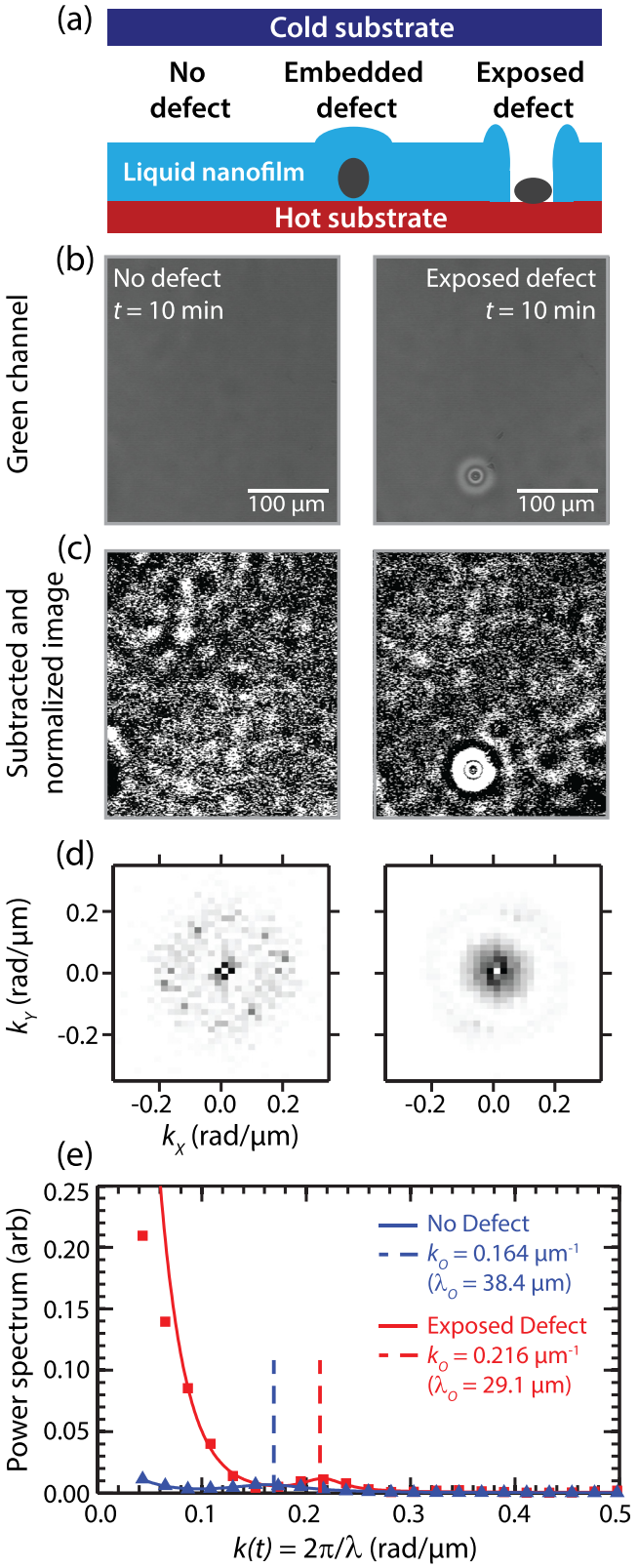

FIG. 5. (a) Sketch illustrating defect-free, embedded defect and exposed defect regions of a liquid nanofilm. (b) Grey scale images from the green channel of experiment #62 in Table VII showing both a defect-free region and a dewetted region caused by an exposed contaminant particle. (c) Corresponding gray scale images after subtraction of reference image $t_{ref} = 3$ min and zeroing of mean intensity value. (d) Corresponding 2D power spectra showing influence of dewetted hole. (e) Corresponding radially averaged and normalized power spectra. Estimates of k_o ($t = 10$ min) and λ_o ($t = 10$ min) obtained from fit to Eq. (1). The dewetted hole led to a smaller estimate of λ_o.

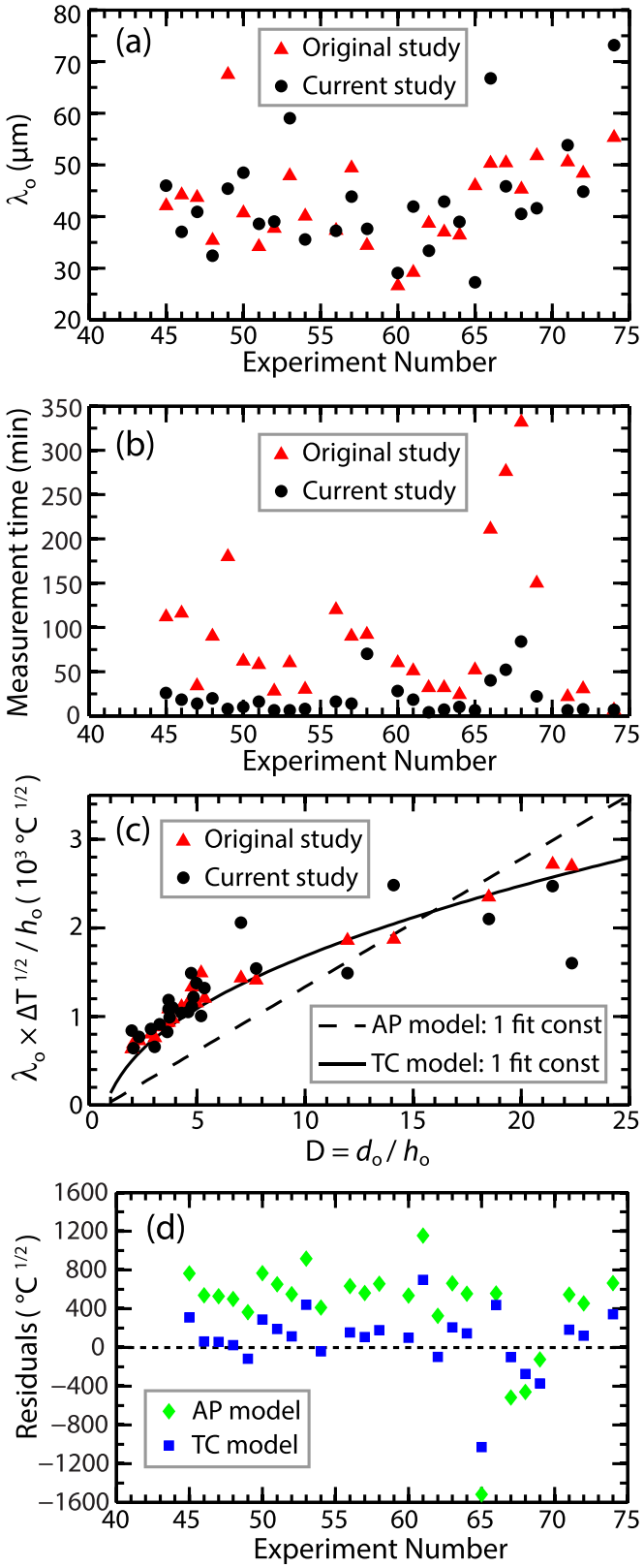

FIG. 6. Comparison between the original[16] and current data sets for λ_o. (a) Extracted values of λ_o for the 26 experiments listed in Table VII. (b) Measurement times for reported values of λ_o. (c) Extracted values of the scaled quantity $\lambda_o \times \sqrt{\Delta T}/h_o$ versus normalized separation distance $D = d_o/h_o$. The solid and dashed lines represent least squares fits to the AP and TC models as described in the text. The fit constants are $C_{AP} = 145\,(^\circ\mathrm{C})^{1/2}$ and $C_{TC} = 576\,(^\circ\mathrm{C})^{1/2}$. (d) Residual values for the fits shown in (c). The sum of squared residuals was computed to be $SSR_{AP} = 1.15 \times 10^7\,^\circ\mathrm{C}$ and $SSR_{TC} = 2.73 \times 10^6\,^\circ\mathrm{C}$.

$$\lambda_o^{\mathrm{AP}} \times \sqrt{\Delta \mathrm{T}}/h_o = C_{\mathrm{AP}}(D + \kappa - 1), \tag{2}$$

and

$$\lambda_o^{\mathrm{TC}} \times \sqrt{\Delta \mathrm{T}}/h_o = C_{\mathrm{TC}}\left(\sqrt{D} + \frac{(\kappa - 1)}{\sqrt{D}}\right). \tag{3}$$

These fit constants were compared to the values derived from the theoretical models, namely,

$$C_{\mathrm{AP}} = 2\pi\sqrt{\gamma u_p/\bar{Q}(1-\kappa)k_{\mathrm{a}}}, \tag{4}$$

and

$$C_{\mathrm{TC}} = 2\pi\sqrt{4\gamma/3\kappa|\partial\gamma\partial \mathrm{T}|}. \tag{5}$$

For consistency in testing the experimental data against the AP and TC model predictions, the input values of the material constants are those listed in Table III. The speed of sound in PS was chosen[24] to be 1300 m/s. For the AP model, the experimental fit constant was computed to be $C_{\mathrm{AP}} = 145$ $(^\circ\mathrm{C})^{1/2}$ while the value computed from Eq. (4) was $C_{\mathrm{AP}} = 111$ $(^\circ\mathrm{C})^{1/2}$. Likewise, the experimental fit constant for the TC model was computed to be $C_{\mathrm{TC}} = 576$ $(^\circ\mathrm{C})^{1/2}$ while that computed from Eq. (5) was $C_{\mathrm{TC}} = 308$ $(^\circ\mathrm{C})^{1/2}$. Although the experimental and theoretical values for the fit constant are much closer in the AP model, the overall functional fit to the current data set is better approximated by the variation in D predicted by the TC model.

Unfortunately, the runs and images which manifested larger defect-free regions are clustered about smaller values of D ranging from about 2 to 8. Those runs correspond to cases in which the instability evolved beneath the cooled SU-8 disk, as depicted in Fig. 2. The experiments for which $D > 10$ contained no disk such that the instability was free to evolve anywhere beneath the larger cold sapphire window. While the linear and curved lines representing the AP and TC models better separate as D increases, experimental difficulties set in once $D > 10$. For example, the larger the value of D, the more difficult it was to level the substrates to ensure parallelism, which in turn led to more uncertainty in the value of d_o and therefore D. That said, the residual values plotted in Fig. 6(d) confirm closer agreement with the TC model. To quantify the quality of fit, we used the sum of squared residuals, here equal to $\mathrm{SSR_{AP}} = 1.15 \times 10^7\,^\circ\mathrm{C}$ versus $\mathrm{SSR_{TC}} = 2.73 \times 10^6\,^\circ\mathrm{C}$.

V. ESTIMATES OF ΔT FROM IMPROVED FINITE ELEMENT MODEL

The temperature difference ΔT between the hot and cold substrates which confine the air/polymer bilayer is a key input parameter for estimating the wavelengths in Tables II and III. In all experiments to date reported in the literate, the separation distance d_o was far too small to accommodate even the smallest of thermocouples, so no direct measurement of ΔT could be made. Descriptions of previous experiments[8–13] suggest that the values of ΔT were *incorrectly* assumed to be the difference in temperature between the set points of the hot and cold stages contacting the two substrates. Such estimates, however, tend to overestimate ΔT. The presence of thin interstitial material layers induced additional thermal resistance, and the many edges which act like thermal fins also induce thermal losses which are not insignificant.

In the original study,[16] finite element simulations[25] were therefore used to obtain estimates of ΔT for each experimental run, namely, $\Delta \mathrm{T} = \mathrm{T}(r = 0, z = 0) - \mathrm{T}(r = 0, z = d_o)$. The experimental system was modeled by a simplified (axisymmetric) geometry consisting only of those material layers in Fig. 7 situated between the two thermocouples shown. Isothermal boundary conditions were imposed along the top of the air layer, $\mathrm{T}(r, z = d_o) = \mathrm{T}_-$, and the bottom of the molten PS nanofilm, $\mathrm{T}(r, z = 0) = \mathrm{T}_+$. The remaining external boundaries of the computational domain were made to coincide with the external edges of each material layer and assumed to be insulating boundaries, thereby subject to vanishing Neumann conditions. The numerical results were calibrated against experiment by ensuring that the temperature recorded by thermocouples placed at two designated locations outside the bilayer region, namely, T_+ and T_- in Fig. 7, matched the numerical estimates. The original estimates for ΔT obtained in this way are designated $\Delta \mathrm{T}^{\mathrm{orig}}$ in Table VII.

In this current revised study, the computational domain was enlarged to include all those material layers shown in Fig. 7 (dimensions listed in Table VI) including the

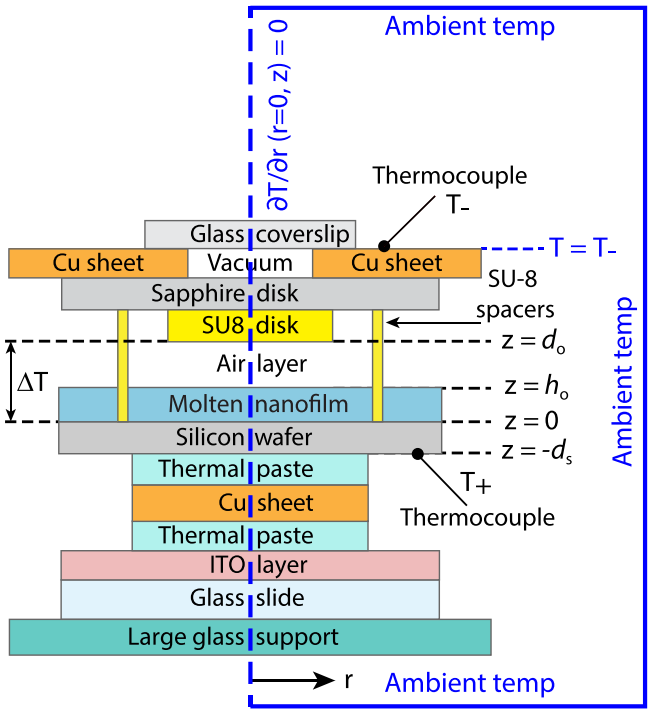

FIG. 7. Axisymmetric geometry for finite element model used to assess steady state temperature distribution within the domain specified by the exterior (blue) boundary (not drawn to scale). Symmetry condition about the vertical axis: $\partial \mathrm{T}\partial r(r = 0, z) = 0$. Isothermal boundary condition $\mathrm{T} = \mathrm{T}_-$ applied to the top surface of the cold Cu sheet beyond the edge of the glass coverslip. The heat per unit volume generated within the ITO layer was modeled by a constant heat generation term, $\dot{\mathrm{Q}}_{\mathrm{ITO}}$, whose value was adjusted until the resulting temperature T_+ matched the thermocouple measurement. Far field isothermal boundary conditions, $\mathrm{T_{amb}} = 23\,^\circ\mathrm{C}$, applied where shown. Table VI lists the dimensions of all domains; Table VII lists the values of T_+, T_-, and $\Delta \mathrm{T}^{\mathrm{curr}}$ for each computational run.

TABLE VI. Dimensions and thermal conductivity values for the material layers shown in Figs. 2 and 7. The thermal conductivity of sapphire was chosen to be 31.0 W/m °C since the orientation axis was unknown (32.7 W/m °C at 45 °C for orientation parallel to c-axis; 30.2 W/m °C at 42 °C for orientation perpendicular to c-axis). The thermal conductivity of ITO typically varies between 4.00 W/m °C and 5.86 W/m °C based on oxygen content, also unknown. A representative value 5.00 W/m °C was therefore used.

Feature	Thickness (mm)	Outer radius (mm)	Thermal conductivity (W/m °C)
Glass coverslip	0.150	14.1	1.10 (23 °C)[26]
Upper (cold) Cu sheet (with 0.5 mm hole)	1.56	50.0	391 (20 °C)[27]
Evacuated air layer (i.e., vacuum)	1.56	0.500	0.0257–0.0454 (20–300 °C)[25]
Cylindrical sapphire window	0.400	3.75	31.0 (42–45)[28]
SU-8 disk	1.38×10^{-3}	0.500	0.300[29]
	1.48×10^{-3}	0.500	0.300[29]
SU-8 spacers (modeled as ring) (width 4.24 μm)	d_o + SU-8 disk thickness	1.504	0.300[29]
Air gap	d_o–h_o (Table VII)	14.1	0.0257–0.0454 (20–300 °C)[25]
PS nanofilm	h_o (Table VII)	14.1	0.130 (100 °C)[19]
Silicon wafer	0.675	14.1	115 (77 °C)[30]
Thermal paste (Omegatherm 201)	0.100	8.75	2.31[31]
Lower (hot) Cu sheet	1.50	8.75	391 (20 °C) [27]
ITO layer	1.50×10^{-4} (Ref. 32)	13.0	5.00[33]
Glass slide	0.700	13.0	1.10 (23 °C)[26]
Glass support	2.00	50.0	1.10 (23 °C)[26]

surrounding air. Far-field isothermal boundary conditions were set to an ambient temperature of 23 °C. The (axisymmetric) computational domain measured 100 mm in radius and 600 mm along the vertical axis. The maximum radial size of the interior material layers was set by the outer radius of the top (cold) Cu sheet and the large (bottom) glass support, both equal to 50 mm. An internal volumetric heat source, $\dot{Q}_{ITO}$, distributed within the volume of the ITO layer, was included in the model to mimic Joule heating from that layer. The isothermal boundary condition applied to the top surface of the top (cold) Cu sheet beyond the edge of the glass coverslip, namely, $T = T_{-}$, acted as the thermal sink to draw heat away from the ITO layer. Conduction was estimated to be the dominant mode of heat transfer throughout the entire system (see discussion below). The equation governing the temperature distribution at steady state operation was therefore given by

$$\nabla \cdot (k_i \nabla T) + \dot{Q}_{ITO} = 0\,, \tag{6}$$

where k_i represents the thermal conductivity of the various elements listed in Table VI and $\dot{Q}_{ITO} = 0$ everywhere except within the ITO layer. All k_i values were assumed to be constant and independent of temperature except for the value of air for which tabulated values as a function of temperature were readily available.

Finite element simulations[25] were conducted using a direct linear solver and Lagrange quadratic elements. Given the large range in material layer thicknesses (ranging from nm to cm), rectangular meshes containing a minimum of five elements were used to span the vertical dimensions of the thinnest domains—these included the ITO, PS, and SU-8 layers. The air layer and SU-8 disk were meshed by free and extremely fine triangular meshes, respectively. All remaining layers were meshed with extremely coarse free triangular meshes modified to have a minimum element size of 0.01 μm, a maximum element growth rate of 1.75, and a resolution of narrow regions of 3. All other meshing parameters were set to extremely coarse defaults. The approximate number of elements was 460 000 with slightly more than 10^6 degrees of freedom.

The actual electrical power per unit volume generated by passage of current to the ITO layer could not be measured in experiment. Instead, the quantity $\dot{Q}_{ITO}$ in Eq. (6) was adjusted for each run until it yielded a match with the temperature T_+ ($r = 13.1$ mm, $z = -d_s$) measured by a thermocouple. The total input power determined in this way generated values between 14.5 W and 31.9 W, well below the 120 W maximum output of the power supply. The resulting values for $\dot{Q}_{ITO}$ are listed in Table VII along with the corresponding solutions for $\Delta T^{curr} = T(r = 0, z = 0) - T(r = 0, z = d_o)$. For experiments #65–69 in Table VII where there was no SU-8 disk, the location $z = d_o$ refers to the bottom surface of the cold sapphire disk.

Fig. 8 shows representative results for the steady state temperature distributions. The parameter values used here are for experiment #56—see Tables VII and VI. Fig. 8(a) illustrates the large variation in mesh sizes needed for the various material layers. The densest meshes overlay the thinnest layers. Fig. 8(b) shows a color map of the temperature distribution matching the two boundary values, $T_+ = 113.0$ °C and $T_- = 35.3$ °C. The region of highest temperature shown in white is due to the ultra low thermal conductivity of the adjacent air, which acts as a thermal insulator. The solid line in Fig. 8(c) depicts the revised temperature profile along the underside of the silicon wafer, $T(r, z = -d_s)$. By contrast, the dashed line represents the isothermal boundary condition enforced in the original study,[16] namely, $T(r, z = -d_s) = T_+$. While the isothermal assumption works well at large radial distances $r > 8$ mm, it fails significantly closer to the central axis $r = 0$. The revised simulations confirm that the Si wafer is significantly cooler than originally believed, consistent with the fact that the overhead SU-8 disk (or sapphire disk when the SU-8 is not present) cools the Si and PS layers beneath it. Shown in Fig. 8(d) are

TABLE VII. Listing of all experiments analyzed along with relevant parameter values for the experimental setup sketched in Fig. 2. Symbol definitions: d_o denotes the separation distance between the proximal hot and cold substrates; h_o is the initial thickness of the PS nanofilm; SU-8 disk thickness refers to the overall separation distance between the hot silicon wafer and the cold sapphire window minus d_o; T_+ and T_- denote the measured thermocouple readings at the locations shown in Fig. 2; Analysis channel refers to the image color channel with the highest contrast (R, G, or B); Image size refers to the image area dimensions; λ_o^{orig}, $t_{\text{meas}}^{\text{orig}}$, and ΔT^{orig}, as well as λ_o^{curr}, $t_{\text{meas}}^{\text{curr}}$, and ΔT^{curr}, denote the original[16] or current values of the fastest growing wavelength measured (meas) at the time indicated, along with the computed values of ΔT from numerical simulations. The time of the reference image used for image subtraction is denoted by $t_{\text{ref.}}$ The power per unit volume for the source term in Eq. (6) is represented by $\dot{Q}_{\text{ITO}}$.

Exp. no.	d_o (nm)	h_o (nm)	SU-8 disk thickness (μm)	T_+ (°C)	T_- (°C)	Analysis channel	Image size $H \times W$ (μm $\times$ μm)	λ_o^{orig} (μm)	$t_{\text{meas}}^{\text{orig}}$ (min)	ΔT^{orig} (°C)	λ_o^{curr} (μm)	$t_{\text{meas}}^{\text{curr}}$ (min)	ΔT^{curr} (°C)	t_{ref} (min)	$\dot{Q}_{\text{ITO}} \times 10^{11}$ (W/m^3)
45	685	186	1.48	113.5	53.4	Blue	297 × 296	42.1	112.0	23.0	46.0	26.0	13.7	16.0	3.45
46	900	189	1.38	114.6	44.6	Blue	312 × 270	44.2	116.0	32.5	37.0	18.0	19.8	4.0	3.89
47	810	189	1.38	114.3	64.8	Blue	270 × 234	43.7	34.0	23.0	40.9	14.0	12.7	12.0	2.85
48	840	183	1.38	112.9	37.0	Blue	234 × 246	35.4	90.0	35.2	32.5	20.0	20.6	14.0	4.24
49	940	181	1.38	114.6	80.2	Blue	354 × 269	67.5	180.0	16.0	45.4	8.0	9.8	4.0	1.95
50	900	181	1.38	113.7	57.1	Blue	246 × 190	40.7	62.0	26.3	48.5	10.0	16.0	2.0	3.17
51	700	181	1.48	113.4	43.9	Blue	310 × 165	34.2	58.0	26.6	38.6	16.0	16.4	2.0	3.95
52	605	185	1.48	114.4	65.4	Blue	196 × 206	37.7	28.0	18.7	39.1	6.0	9.8	4.0	2.89
53	865	183	1.38	114.4	68.5	Blue	401 × 253	47.9	60.0	21.3	59.1	6.0	12.4	4.0	2.62
54	670	185	1.48	114.3	66.1	Blue	243 × 270	40.1	30.0	18.4	35.6	8.0	10.6	6.0	2.80
56	885	183	1.38	113.0	35.3	Blue	318 × 290	37.3	120.0	36.1	37.2	16.0	22.1	4.0	4.30
57	690	185	1.48	114.5	68.7	Blue	341 × 296	49.4	90.0	17.5	43.9	14.0	10.3	6.0	2.66
58	760	142	1.48	113.9	55.6	Green	243 × 144	34.4	92.0	24.8	37.6	70.0	15.0	10.0	3.27
60	735	95	1.48	114.0	54.5	Blue	179 × 191	26.6	60.0	25.4	29.1	28.0	15.5	5.0	3.33
61	710	101	1.48	113.9	54.9	Green	270 × 296	29.2	51.0	24.6	42.0	18.0	14.9	9.0	3.32
62	785	258	1.48	113.9	49.1	Green	291 × 333	38.7	32.0	25.6	33.4	4.0	15.7	3.0	3.67
63	740	201	1.48	114.1	49.8	Blue	158 × 163	37.0	32.0	25.8	42.9	7.0	15.5	6.0	3.64
64	615	215	1.48	114.2	49.2	Blue	261 × 325	36.4	24.0	22.4	39.0	10.0	13.0	6.0	3.79
65	2100	94	0	114.8	71.8	Blue	396 × 305	46.0	52.0	30.4	27.3	6.0	17.8	0.0	2.48
66	2200	156	0	114.7	66.7	Blue	185 × 174	50.3	211.0	33.7	66.8	40.0	20.3	2.0	2.73
67	2360	110	0	114.6	66.1	Blue	369 × 246	50.4	276.0	35.2	45.9	52.0	21.7	40.0	2.66
68	2350	127	0	114.4	53.0	Blue	239 × 225	45.3	332.0	43.4	40.5	84.0	27.6	4.0	3.34
69	2200	184	0	114.2	53.3	Blue	539 × 492	51.8	150.0	43.6	41.6	22.0	25.8	14.0	3.44
71	850	366	1.48	115.2	46.2	Blue	252 × 239	50.6	21.7	27.5	53.8	6.5	16.4	5.0	3.92
72	680	331	1.48	115.3	47.2	Blue	189 × 203	48.4	30.7	22.4	44.8	7.3	13.1	4.3	3.98
74	770	390	1.48	114.3	58.2	Blue	188 × 195	55.3	6.7	20.0	73.2	6.7	11.5	5.0	3.28

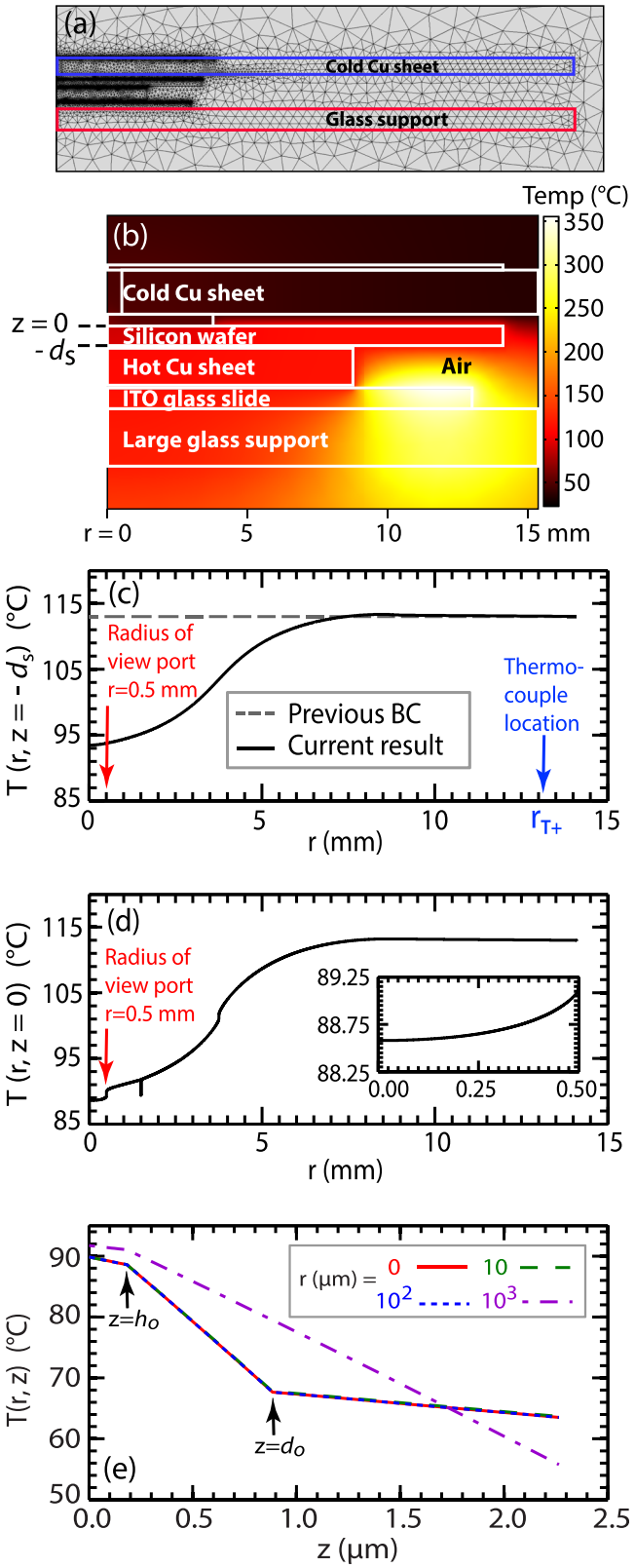

FIG. 8. (a) Sample finite element mesh for domains in Fig. 7. (b) Steady state thermal distribution for experiment #56 (drawn to scale). (c) Solid line = T(r, $z = -d_s$) (underside of Si wafer) showing current result. Dashed line = isothermal boundary condition T(r, $z = -d_s$) = T_+ used in previous simulations.[16] (d) Solid line = T(r, $z = 0$) (along PS/Si interface). Jump at $r = 0.5$ mm due to edge of perforated hole (view port) in top (cold) Cu sheet shown in Fig. 7. Dip at $r = 1.5$ mm due to SU-8 spacer. Jump at $r = 3.75$ mm due to sapphire disk edge. Inset: Magnified view of T($0 \le r \le 0.5$ mm, $z = 0$) (region within view port). (e) T(r, z) for $r = 0$, 10, 10^2, and 10^3 μm.

results of the temperature profile along the Si/PS interface, T(r, $z = 0$). The inset is a magnified view of the temperature change within the radius defined by the view port (i.e., circular perforation) in the top (cold) Cu sheet, namely, T($0 \le r \le 0.5$ mm, $z = 0$). The maximum difference is less than 0.5 °C. Shown in Fig. 8(e) is also the temperature variation along the vertical direction for various radial distances $r = 0$, 10, 10^2, and 10^3 μm. Superimposed on the data are the locations of the air/PS interface at $z = h_o$ and the bottom of the (cold) SU-8 disk at $z = d_o$. The data for radii $r \le 100$ μm collapse onto a common curve, indicating that the value of $\Delta T = T(r = 0, z = 0) - T(r = 0, z = d_o)$ is insensitive to the radial distance from the central axis $r = 0$ for $r < 100$ μm.

The linear stability calculations for the AP and TC models predicate a fluid base state exposed to a large transverse thermal gradient but no lateral gradient. For the results shown in Fig. 8(d), the estimated maximum radial thermal gradient was 1.6×10^3 °C/m, based on a maximum temperature increase of 0.8 °C over a radial distance of 0.5 mm. The estimated maximum vertical thermal gradient was 2.5×10^7 °C/m based on a maximum vertical difference of 22.1 °C at $r = 0$ over a vertical gap spacing of $d_o = 885$ nm. Consequently, the lateral thermal gradient was roughly four orders of magnitude smaller than the vertical gradient and therefore completely negligible. These estimates were typical of all runs conducted and confirmed the assumptions inherent in the AP and TC models.

Estimates were also used to confirm that thermal conduction was the dominant mechanism of heat transfer in the experimental system modeled. The Rayleigh number for the domain comprising the thin air layer just above the liquid nanofilm was estimated to be four orders of magnitude smaller than the critical number required for convective instability. Likewise, an estimate for the domain along the vertical edge of the hot Cu sheet above the ITO layer yielded a Rayleigh number roughly three orders of magnitude smaller than required for convection. Separate estimates confirmed that the thermal flux due to radiative losses was at least an order of magnitude smaller than convective losses. As a result, the heat generated by the ITO layer was assumed to distribute throughout the system solely by thermal conduction.

The numerical model described provided more accurate estimates of the input parameter ΔT required for assessing the fastest growing wavelength predicted by the AP and TC models. Fig. 9(a) shows a direct comparison of ΔT obtained from the original and revised simulations. The current study generated lower average values for ΔT, i.e., $\Delta T_{avg}^{orig} = 26.9$ °C versus $\Delta T_{avg}^{curr} = 16.1$ °C. Fig. 9(b) shows the comparison between theory and experiment for the AP and TC model predictions based on Eqs. (2) and (3) using a single fit constant for each. Here, λ_o denotes values reported in the original study[16] while ΔT denotes current values based on the revised simulations. The original values of λ_o were input here in order to discern separately the influence of revisions to λ_o and ΔT. The fit constants were found to be $C_{AP} = 123\,°C^{1/2}$ and $C_{TC} = 471\,°C^{1/2}$. These numerical values exceed the theoretical values from Eqs. (4) and (5) by 10% and 53%, respectively. Fig. 9(c) depicts the corresponding residual values.

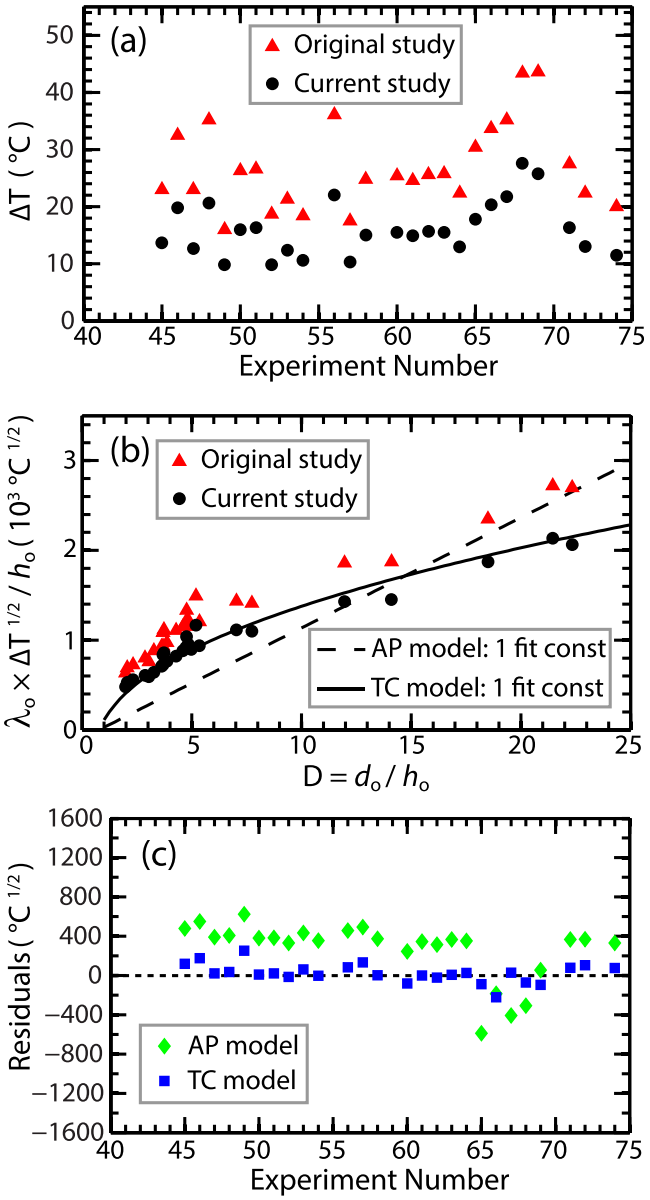

FIG. 9. (a) Comparison of the temperature differences, $\Delta T = T(r = 0, z = 0) - T(r = 0, z = d_o)$, computed from the original[16] (triangles) and current numerical model (circles) for the experiments listed in Table VII. The complete set of experimental and simulation parameters can be found there and in Table VI. (b) Comparison of the original to current results for the scaled quantity $\lambda_o \times \sqrt{\Delta T}/h_o$ versus the normalized separation distance $D = d_o/h_o$. Here, λ_o refers to the original values reported previously[16]—ΔT denotes the values computed in the current study [plotted in (a)]. The dashed line is a least squares fit to the AP model with a single fit constant $C_{AP} = 123\,^{\circ}C^{1/2}$; the solid line is a least squares fit to the TC model with a single fit constant $C_{TC} = 470\,^{\circ}C^{1/2}$. (c) Residual values for the fits shown in (b). The sum of squared residuals was computed to be $SSR_{AP} = 4.12 \times 10^6\,^{\circ}C$ and $SSR_{TC} = 2.42 \times 10^5\,^{\circ}C$.

Computation of the sum of squared residuals, namely, $SSR_{AP} = 4.11 \times 10^6\,^{\circ}C$ and $SSR_{TC} = 2.43 \times 10^5\,^{\circ}C$, nonetheless, supports a better functional fit to the TC model albeit the fit constant is roughly 50% larger than the theoretical estimate.

VI. COMBINED EFFECT OF IMPROVED ESTIMATES FOR λ_o AND ΔT

In Secs. IV and V, we *separately* examined the influence of improvements to λ_o and ΔT. Here, we report the final combined results of these two improvements. Fig. 10(a) shows a direct comparison of the rescaled quantity $\lambda_o \times \sqrt{\Delta T}/h_o$ versus normalized separation distance D between the original and current data sets. The solid and dashed lines represent least squares fits to the data based either on one or no fit constant according to Eqs. (2) and (5). The best fit constants were estimated to be $C_{AP} = 112\,^{\circ}C^{1/2}$ and $C_{TC} = 447\,^{\circ}C^{1/2}$, exceeding the theoretical estimates computed from Eqs. (4) and (5) by 1% and 45%, respectively. The fact that the fitted and predicted coefficient values for C_{AP} are essentially equal, however, does not indicate closer agreement with the AP model since the functional dependence of the data on D is not well captured by that model.

To highlight this point, we show in Fig. 10(b) the corresponding residual values, i.e., the square of the deviation between the data and fitted curve (TC) or line (AP). Clearly, the residual values for the TC model are closely distributed about zero, which indicates a better fit to the functional

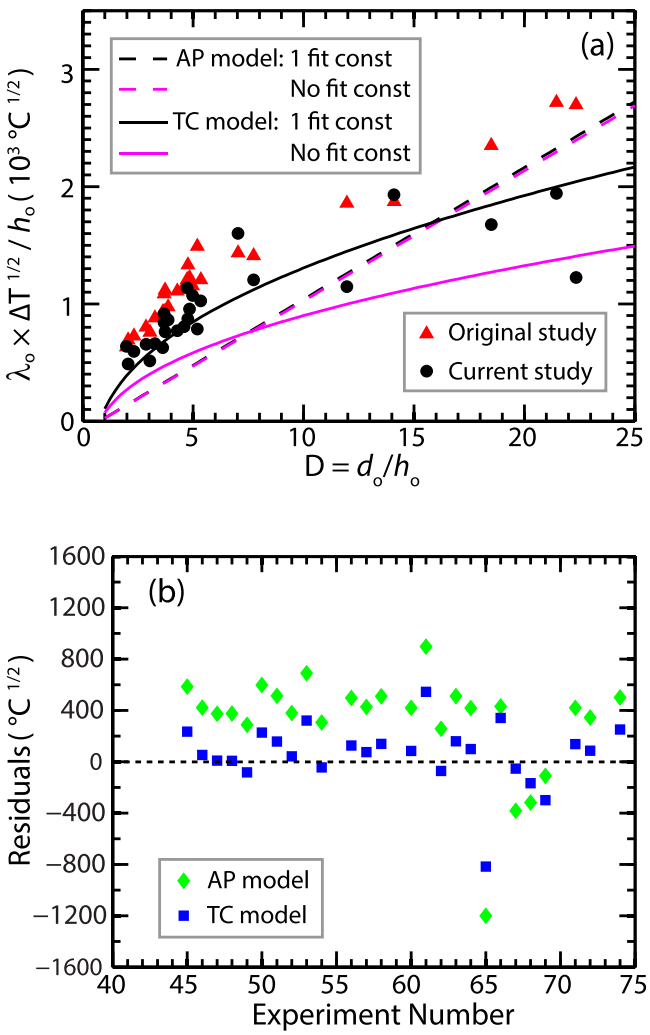

FIG. 10. (a) Comparison of the original and current data sets for the scaled quantity $\lambda_o \times \sqrt{\Delta T}/h_o$ versus normalized separation distance D. Here, λ_o and ΔT denote the improved values reported in this current work. The fit constant for the AP model is $C_{AP} = 112\,^{\circ}C^{1/2}$; the value estimated directly from Eq. (4) is $111\,^{\circ}C^{1/2}$. The fit constant for the TC model is $C_{TC} = 447\,^{\circ}C^{1/2}$; the value estimated directly from Eq. (5) is $308\,^{\circ}C^{1/2}$. (b) Residual values for the one fit constant curves shown in (a). The sum of squared residuals is $SSR_{AP} = 6.84 \times 10^6\,^{\circ}C$ and $SSR_{TC} = 1.63 \times 10^6\,^{\circ}C$.

dependence on D. The sum of squared residuals, namely, $SSR_{AP} = 6.84 \times 10^6\,^{\circ}C$ versus $SSR_{TC} = 1.63 \times 10^6\,^{\circ}C$, confirms that the TC model more closely replicates the functional behavior with D measured experimentally.

A comparison (not shown) of the best fit TC curve in Fig. 10(a) with the corresponding curve in Fig. 4(a) of Ref. 16 reveals that the improved image analysis routines of this current study, however, do yield increased scatter in the data. This is because the extraction of λ_o at much earlier times relies on noisier data sets in which emergent features are yet so pronounced. This is evident from the sample images and wavenumber values shown in Figs. 3(b) and 3(e) and Figs. 4(b) and 4(e). The significant difference in extraction times for λ_o between the current and original studies are listed in Table VII, i.e., t^{curr}_{meas} versus t^{orig}_{meas}. Despite the increased scatter, however, the fit constant for the improved data sets is closer to the theoretical estimate of $C_{TC} = 308\,^{\circ}C^{1/2}$—that is, the best fit (not shown) to the data (triangles) from the original study yielded $C_{TC} = 607\,^{\circ}C^{1/2}$, while the best fit to the improved data (solid dots) shown in Fig. 10(a) yields $C_{TC} = 447\,^{\circ}C^{1/2}$.

VII. DISCUSSION OF EXPERIMENTAL CHALLENGES

The combined results of the current study shown in Fig. 10 indicate closer agreement with the functional form predicted by the TC model. Unfortunately, the data are clustered mostly about smaller values of $D \leq 8$. The analytic expressions in Eqs. (2)–(5) clearly show that the models more strongly differentiate for larger values of D. We are currently redesigning the experimental system in order to access larger substrate separation distances more easily and with higher reproducibility.

Both the AP and TC models predicate certain conditions which must be satisfied by experiment. These include a liquid nanofilm of constant viscosity, parallelism of the substrates confining the air/liquid bilayer, an initial flat and uniform liquid film, a substrate separation distance characterized by the slender ratio $(d_o/\lambda_o)^2 \ll 1$, heat transfer dominated by thermal conduction, and infinitesimally small fluctuation amplitudes to satisfy the condition of *linear* instability. As an aside, if the latter condition is satisfied, then so too is the assumption of constant viscosity since the interface is infinitesimally close to its original position and therefore the film viscosity about the same as that of the original film.

To minimize misalignment from bow and warp of the silicon and sapphire layers and to enhance parallelism of the confining substrates, the interference fringes arising from non-parallel substrates were monitored and leveling screws adjusted accordingly. Film uniformity and flatness were maximized by conducting ellipsometric measurements of film thickness shortly after the polymer films were spun coat onto the silicon substrates. For each experiment listed in Table VII, we also confirmed that the slender gap approximation was well satisfied by ratios estimated to be less than 10^{-4}. As reported in Sec. V, we also checked that the thermal flux due to conduction far outweighed thermal flux losses due to natural convection or radiation. Finally, as described earlier in this paper, the substantial improvements to the image analysis allowed extraction of λ_o at much earlier times than originally reported. All in all, these checks ensured that the assumptions inherent in the theoretical models were fairly well satisfied in experiment.

Direct comparison of experiment to theory was nonetheless challenging. In particular, the influence of dust particles and other film imperfections is particularly deleterious in liquid nanofilms. For example, contaminant particles were sometimes trapped unintentionally beneath the SU-8 spacers used to preset the values of D. This problem led to underestimates in the value of D, as well as non-parallelism. Despite the rigidity of SU-8 after baking, there was also a concern that the spacers might have undergone some compression during loading and leveling followed by expansion during heating, leading to uncertainty in the exact values of D.

An additional but small uncertainty in the numerical estimates of ΔT was also incurred since the *exact* location of the thermocouple denoted by T_+ in Fig. 7 was not known precisely. Furthermore, the actual silicon wafer substrates were square and not cylindrical, as modeled in the simulations. Finally, the layer of thermal paste between the silicon wafer and hot copper sheet used to enforce good thermal contact had to be applied anew for each experimental run. The thickness of this paste was not necessarily equal from run to run and the volume dispensed was not measured so the thickness of that layer was somewhat uncertain.

Small additional uncertainties were also likely incurred in having to rely on literature values for material constants, as listed in Tables II and III. While the values of the surface tension, γ, and the temperature coefficient, γ_T, from Ref. 19 were interpolated with respect to temperature and linearly extrapolated with respect to molecular weight to better match the actual liquid films used experimentally, other film constants like the thermal conductivity, k_p, and the speed of sound, u_p, contained no information about the polymer molecular weight but were used as reported. There remains of course some uncertainly as well with regard to the fact that the literature values reported in Tables II and III refer to measurements made on bulk samples, which may not always properly reflect the values pertinent to nanofilms where large surface to volume ratios can influence material constants.

VIII. CONCLUSION

In this paper, we have reanalyzed the experiments reported in McLeod *et al.*[16] in order to obtain improved estimates for λ_o, the wavelength of the fastest growing mode, and ΔT, the temperature drop across the air/nanofilm bilayer. Accurate values of these two key parameters are necessary for making contact with theoretical predictions in order to identify the mechanism leading to instability in flat nanofilms subject to a large applied transverse thermal gradient. The AP model ascribes periodic film deformation due to buildup of acoustic phonon pressure within the nanofilm caused by the reflection of long wavelength phonons from interfaces within the confined bilayer. The TC model ascribes periodic film deformation to thermocapillary forces acting along the air/nanofilm interface which draw alternating portions of the liquid film toward the cooler substrate.

As detailed in this paper, the improved image analysis for λ_o allowed extraction of emergent features at much earlier times of the instability than previously reported. In addition, the revised thermal simulations described, which better mimic the actual experimental system, led to smaller estimated values of ΔT. Refinement of these two parameter values leads to closer overall agreement with the predictions of the TC model rather than the AP model. In particular, the experimental data more closely follow the functional dependence on the normalized substrate separation distance $D = d_o/h_o$ described by the thermocapillary mechanism. However, the best fit to both models still requires one fit constant. While the value of that constant for the AP model is very close to its theoretical value, the same is not true for the TC model for which the fit constant is approximately 50% larger than the theoretical value. We have discussed several possible causes for this discrepancy. In an effort to resolve this problem, we are currently redesigning the entire experimental system in the hope of conclusively differentiating between the acoustic phonon and thermocapillary mechanisms.

ACKNOWLEDGMENTS

This work was supported by a NASA Space Technology Research Fellowship (KRF). The authors also extend their appreciation to Dr. Euan McLeod for helpful discussions and useful notes he provided regarding the original experiments.

[1]L. Trefethen, *Surface Tension in Fluid Mechanics* (National Committee for Fluid Mechanics Films, 1969).
[2]K. A. Smith, J. Fluid Mech. **24**, 401 (1966).
[3]S. H. Davis, Annu. Rev. Fluid Mech. **19**, 403 (1987).
[4]S. J. VanHook, M. F. Schatz, W. D. McCormick, J. B. Swift, and H. L. Swinney, Phys. Rev. Lett. **75**, 4397 (1995).
[5]S. J. VanHook, M. F. Schatz, J. B. Swift, W. D. McCormick, and H. L. Swinney, J. Fluid Mech. **345**, 45 (1997).
[6]M. Dietzel and S. M. Troian, J. Appl. Phys. **108**, 074308 (2010).
[7]P. Deshpande, X. Sun, and S. Y. Chou, Appl. Phys. Lett. **79**, 1688 (2001).
[8]S. Y. Chou and L. Zhuang, J. Vac. Sci. Technol., B **17**, 3197 (1999).
[9]L. Zhuang, "Controlled self-assembly in homopolymer and diblock copolymer," Ph.D. thesis (Princeton University, Princeton, NJ, 2002).
[10]E. Schäffer, "Instabilities in thin polymer films: Structure formation and pattern transfer," Ph.D. thesis (Konstanz University, 2001).
[11]E. Schäffer, S. Harkema, R. Blossey, and U. Steiner, Europhys. Lett. **60**, 255 (2002).
[12]E. Schäffer, S. Harkema, M. Roerdink, R. Blossey, and U. Steiner, Adv. Mater. **15**, 514 (2003).
[13]E. Schäffer, S. Harkema, M. Roerdink, R. Blossey, and U. Steiner, Macromolecules **36**, 1645 (2003).
[14]M. Dietzel and S. M. Troian, Phys. Rev. Lett. **103**, 074501 (2009).
[15]M. Dietzel and S. M. Troian, in *Materials Systems and Processes for Three Dimensional Micro- and Nanoscale Fabrication and Lithography*, edited by S. M. Kuebler and V. T. Milam (Materials Research Society, 2009), Vol. 1179E, pp. 1179–BB08–02.
[16]E. McLeod, Y. Liu, and S. M. Troian, Phys. Rev. Lett. **106**, 175501 (2011).
[17]E. McLeod and S. M. Troian (unpublished).
[18]*CRC Handbook of Chemistry and Physics*, edited by D. R. Lide, 81st ed. (CRC Press, Boca Raton, 2000).
[19]Z. Pu, in *Polymer Data Handbook*, edited by J. E. Mark (Oxford University Press, New York, 1999).
[20]J. R. Welty, C. E. Wicks, and R. E. Wilson, *Fundamentals of Momentum, Heat, and Mass Transfer*, 3rd ed. (John Wiley & Sons, 1984).
[21]O. Urakawa, S. F. Swallen, M. D. Ediger, and E. D. von Meerwall, Macromolecules **37**, 1558 (2004).
[22]MATLAB, version 8.1.0 (R2013a), The MathWorks Inc., Natick, MA, 2013.
[23]F. J. Harris, Proc. IEEE **66**, 51 (1978).
[24]A. Naranjo, M. del Pilar Noriega, T. Osswald, A. Roldan-Alzate, and J. D. Sierra, *Plastics Testing and Characterization: Industrial Applications* (Carl Hanser Verlag, Munich, 2008).
[25]COMSOL, Inc., COMSOL Mutliphysics®, Los Angeles, CA.
[26]Corning, Inc., *Corning® Eagle XG®*, Corning, NY.
[27]McMaster-Carr Supply Co., *Multipurpose 110 Copper*, Santa Fe Springs, CA.
[28]Y. S. Touloukian, R. W. Powell, C. Y. Ho, and P. G. Klemens, *Thermal Conductivity—Nonmetallic Solids*, Thermophysical Properties of Matter Vol. 2 (IFI/Plenum, New York, 1970).
[29]MicroChem Corp., *SU-8 2000 Epoxy Photoresist*, Westborough, MA.
[30]W. Fulkerson, J. P. Moore, R. K. Williams, R. S. Graves, and D. L. McElroy, Phys. Rev. **167**, 765 (1968).
[31]OMEGA Engineering, Inc., *OMEGATHERM® 201*, Stamford, CT.
[32]Delta Technologies, Ltd., *Part No. CB-50IN-S205*, Loveland, CO.
[33]T. Ashida, A. Miyamura, N. Oka, Y. Sato, T. Yagi, N. Taketoshi, T. Baba, and Y. Shigesato, J. Appl. Phys. **105**, 073709 (2009).